ENGINEERING

Seizure detection via reservoir computing in MoS_2-based charge trap memory devices

Matteo Farronato[1]*, Piergiulio Mannocci[1], Alessandro Milozzi[1], Christian Monzio Compagnoni[1], Alessandro Barcellona[2], Andrea Arena[3], Marco Crepaldi[2], Gabriella Panuccio[3], Daniele Ielmini[1]*

Neurological disorders are a substantial global health burden, affecting millions of people worldwide. A key challenge in developing effective treatments and preventive measures is the realization of low-power wearable systems with early detection capabilities. Traditional strategies rely on machine learning algorithms, but their computational demands often exceed what miniaturized systems can provide. Neuromorphic computing, inspired by the human brain, demonstrated capabilities of on-chip computing with low power consumption. In this context, bidimensional (2D) semiconductors hold notable promise, thanks to their unique electronic properties, atomic-scale thickness, and scalability, making them ideal for low-power applications. This work presents a neuromorphic reservoir computing system exploiting MoS_2-based charge trap memories (CTMs) for processing of electrophysiological signals. Real-time seizures detection is achieved, thanks to the nonlinear integration of local-field potential (LFP) recorded from in vitro rodent models of ictogenesis. The results support MoS_2-based CTMs for low-power biomedical devices in clinical diagnosis and treatment of epilepsy.

INTRODUCTION

Epilepsy is a chronic neurological disorder characterized by the enduring predisposition of the brain to generate abnormal electrical discharges (seizures), which cause the loss of control of body functions. Epilepsy affects 2% of the global population (*1*), of which >30% is medically intractable (*2*, *3*), falling into the drug-resistant epilepsy (DRE) category. Epilepsy can be debilitating and life threatening and it is often accompanied by psychiatric and cognitive comorbidities that portray a notable societal problem, which significantly contribute to the global burden of disease of chronic brain disorders. Thus, it is essential to develop new treatment strategies which go beyond the conventional antiseizure medications. Among all, closed-loop deep brain stimulation (DBS) is attracting interest thanks to its demonstrated efficacy in decreasing seizure frequency and severity, as well as its tolerability and low risks (*4*, *5*). Closed-loop DBS systems generally include (i) a sensor to record signals from the patient's brain, (ii) a processor to analyze those signals, and (iii) an actuator to deliver electrical stimulation based on the processed signals. Recently, automatic seizure detectors have been demonstrated using software-based machine learning algorithms and artificial neural networks (*6*, *7*). These detection approaches are computationally complex and must often run on high-performance computers, limiting their use to the offline mode. To overcome these limitations, hardware solutions based on field-programmable gate arrays (FPGAs) (*8*, *9*), application-specific integrated circuits (ASICs) (*10*) and systems-on-chip (SoC) (*11*, *12*) have been proposed. However, these hardware systems generally require the digitalization, transmission, and processing in an external system based on conventional computers running artificial intelligence accelerators for data analysis (*13*). Conversion, transmission, and storage of these data raise severe power and throughput constraints (*14*, *15*) while cloud-based data processing involves an energy- and time-consuming computation within a deep neural network (DNN). This conventional methodology prevents (i) a real-time analysis of neural signals for prompt seizure detection and electrical stimulation and (ii) a low-energy consumption, which is crucial for battery-powered systems aiming at implantable and wearable electronics.

In this context, a promising solution to reduce energy consumption and enable local, on-chip analysis of neural signals is neuromorphic computing, where data are processed locally, close to the sensor and consuming only low power. An important subset of neuromorphic computing concepts is reservoir computing (RC), consisting of a three-layer architecture with an input (sensing) layer, a hidden (processing) layer typically defined by some nonlinear recurrent network dynamics and an output (classification) layer (*16*). To mimic the locality and adaptability of human brain data processing, neuromorphic computing can leverage the properties of various types of memristive devices capable of emulating various biophysical phenomena, such as synaptic plasticity, short-term memory, and neuron integration, via device physics (*17*). In the literature, one-transistor-one-resistor (1T1R) memristors (*8*, *18*), ferroelectric field-effect transistors (*19*), dynamic memristors (*12*, *20*), and even optoelectronic devices (*21*, *22*) have been successfully applied in RC tasks. Bidimensional (2D) semiconductors such as molybdenum disulfide (MoS_2) have also been extensively studied for neuromorphic processing. 2D semiconductors enable atomic-scale thickness, good carrier mobility, and cost-effective integration schemes (*23*, *24*), thus attracting interest as active materials for future complementary metal-oxide semiconductor (CMOS) technologies (*25*, *26*). Various types of MoS_2-based memory devices have been proposed, including floating gate memories (*27*), memristors (*28*), and memtransistors (*29*, *30*). Recently, a MoS_2-based charge trap memory (CTM) was reported (*31*). This device has a MOSFET-like structure and relies on charge trapping/detrapping at the interface between the MoS_2 channel and the SiO_2 insulator to achieve memory operation. The charge trapping/detrapping phenomena are triggered by voltage pulses applied to the gate or the drain of the device and cause a change of its

[1]Dipartimento di Elettronica, Informazione e Bioingegneria, Politecnico di Milano and IU.NET, Piazza Leonardo da Vinci 32, 20133 Milano, Italy. [2]Electronic Design Laboratory, Istituto Italiano di Tecnologia, Via Enrico Melen 83, 16152 Genova, Italy. [3]Enhanced Regenerative Medicine Laboratory, Istituto Italiano di Tecnologia, Via Morego 30, 16163 Genova, Italy.
*Corresponding author. Email: matteo.farronato@polimi.it (M.F.); daniele.ielmini@polimi.it (D.I.)

threshold voltage V_T, hence of its drain current I_D and device conductance G. RC with this MoS_2-based CTM was demonstrated for classification of simple images, taking advantage of its nonlinear potentiation/depression response and of its low current, thanks to subthreshold bias operation (*31*). However, the performance and potential of MoS_2-based CTMs for neural signal processing have not been shown yet.

Here, we propose a system for real-time neuromorphic processing of electrophysiological signals with MoS_2-based CTMs (Fig. 1). After a preprocessing stage including amplification with low-noise amplifiers (LNAs) and multiplexing, the signals are applied to a reservoir layer where they are nonlinearly integrated by MoS_2-based CTMs with short-term memory. The output of the reservoir layer is then submitted to a readout layer, consisting of a simple threshold detection stage for signal classification. Real-time detection and classification of seizure-like activity in in vitro rodent models of ictogenesis is demonstrated, supporting the MoS_2-based CTM for low-power biomedical devices for research in epilepsy diagnosis and treatment.

RESULTS

Experimental devices and trapping/detrapping dynamics

Figure 2A illustrates the MoS_2-based CTM device, featuring metal drain and source terminals deposited on a 2D semiconductor channel with back-gated structure (*24*, *31*). The channel was obtained by mechanical exfoliation of monocrystalline MoS_2 flakes with a typical thickness of about five monolayers on an oxidized silicon substrate. The Au source and drain terminals were deposited by thermal evaporation and patterned by electron beam lithography. Figure 2B shows the scanning electron microscopy (SEM) image of the structure, indicating a channel length $L_{channel}$ = 100 nm. Figure 2C shows the measured I_D-V_G transcharacteristic of 16 devices (see also fig. S1), showing a high on-off I_D ratio of about 10^6 and a negative native V_T of about −5 V. The large values of V_G in the test are due to the relatively thick SiO_2 layer adopted in the samples, equal to 90 nm. All devices display a clockwise hysteresis that can be explained by charge trapping/detrapping at the interface between the SiO_2 layer and the MoS_2 channel or within bulk SiO_2 traps during the forward/reverse V_G sweep (*31*–*34*). Electron trapping over the forward V_G sweep causes a positive V_T shift, as sketched in Fig. 2D. Conversely, electron detrapping over the negative V_G sweep causes a negative V_T shift, as shown in Fig. 2E. Charge retention is limited to a timescale in the range of few seconds, thus enabling short-term memory for application in RC. As demonstrated in our previous work (*31*), the hysteretic behavior of the device remains consistent throughout repeated cycles, underscoring its robustness for real-time neuromorphic applications. To further strengthen the device stability, a passivation layer can be added to protect the MoS_2 channel from air exposure. Figure S2 presents the I_D-V_G curve of a CTM device with a 100-nm-thick Al_2O_3 layer deposited on top of the channel. The hysteretic characteristic of the device is similar to the one shown in fig. S1 for a nonpassivated device, except for a negative shift of the threshold voltages. For this reason, and also to simplify the fabrication process, all experiments in this work were conducted using nonpassivated devices.

To better understand the hysteretic and short-term memory behaviors, we conducted an extensive pulsed characterization of the MoS_2-based CTMs. Figure 3A shows a schematic representation of the device and of the voltages applied in the test. The source and drain terminals are always kept at 0 and 0.1 V, respectively. I_D is measured at a reference gate read voltage $V_{G,read}$, usually in the subthreshold regime to minimize power consumption (*35*). To trigger device potentiation, gate voltage pulses of amplitude $\Delta V_{G,pulse}$ (evaluated with respect to $V_{G,read}$) and duration Δt_{pulse} are applied in sequence. Figure 3B shows an example of the V_G waveform resulting from this test scheme (the example refers to the case of $V_{G,read} = -7$ V, $\Delta V_{G,pulse} = -3$ V, $\Delta t_{pulse} = 50$ ms, and read period $\Delta t_{read} = 50$ ms). Figure 3C shows the related behavior of I_D along the test, revealing a gradual increase in the current corresponding to synaptic potentiation (*33*). After the applied pulse sequence, I_D decays in time due to the spontaneous charge trapping process. Figure 3D shows channel conductance $G = I_D/V_{DS}$ as a function of the number of applied pulses, for increasing $|\Delta V_{G,pulse}|$. A higher $|\Delta V_{G,pulse}|$ causes stronger potentiation. The slowdown and saturation in the growth of G observed for increasing number of pulses at high $|\Delta V_{G,pulse}|$ can be explained

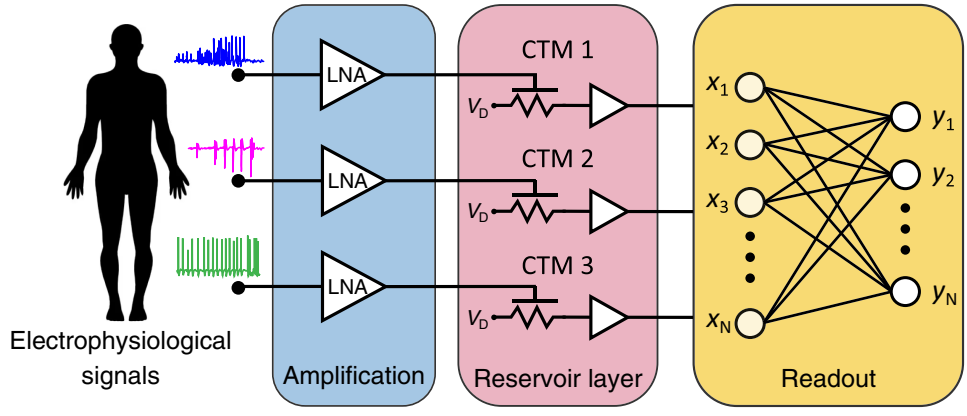

Fig. 1. Generalized, schematic illustration of a RC system with MoS_2-based CTM devices for seizure detection. Electrophysiological signals are first preprocessed in the analog domain for amplification through LNAs, filters, and other types of preconditioning elements. The reservoir layer includes the MoS_2-based CTM devices responsible for feature extraction from the input signals, e.g., signals coming from several locations within the brain slice or the same signal after different types of preprocessing functions, e.g., a positive and negative amplification or band-pass filtering over various frequency ranges. The response of the CTM devices is lastly processed by the readout layer for signal classification and seizure detection. The readout layer is represented as a fully connected neural network, although it can consist of any type of machine learning algorithm, e.g., decision tree, SVM, or a simple threshold comparator depending on the complexity of classification.

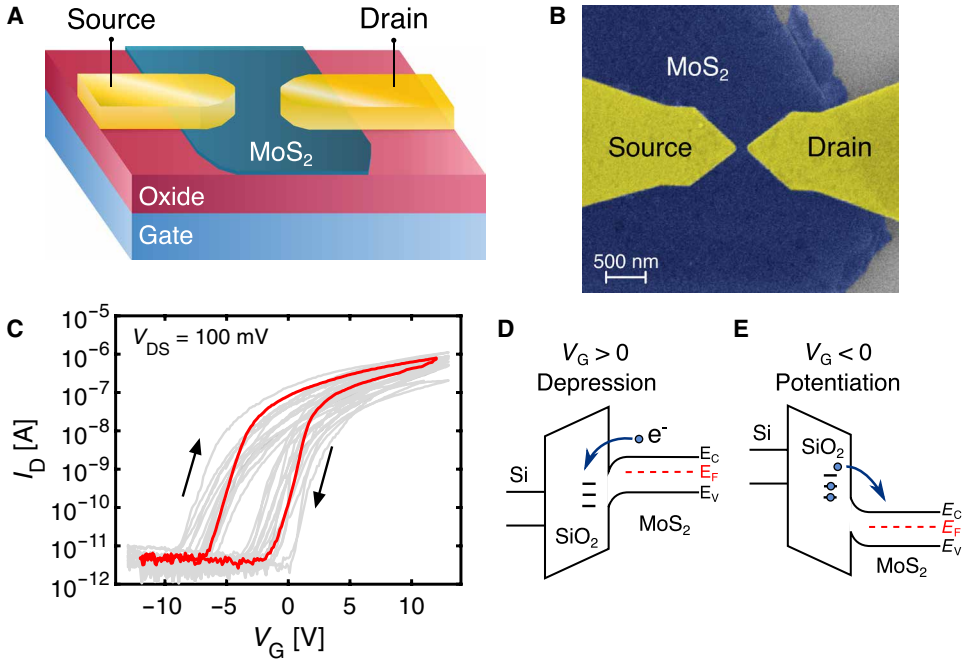

Fig. 2. MoS_2 CTM. (**A**) Graphical representation of the MoS_2-based CTM, with Au source and drain terminals deposited on top of the 2D channel. (**B**) Scanning electron microscopy (SEM) image of the device (scale bar 500 nm). (**C**) Measured I_D-V_G transcharacteristics at V_{DS} = 100 mV for CTM devices with SiO_2 thickness t_{ox} = 90 nm, as obtained from forward and reverse V_G sweep. To prove the reproducibility of the results, the figure reports the curves of 16 devices with one of them highlighted in red. The clockwise hysteresis is due to the presence of traps at the interface between the oxide and the 2D semiconductor, which cause threshold drift as a function of the gate polarization. The sweep rate was 1.05 V/s. (**D**) Band diagram for positive V_G and (**E**) band diagram for negative V_G, showing the charge trapping and detrapping processes at the origin of the depression and potentiation dynamics of the CTM device.

as the outcome of the combined effect of the electrostatic feedback and of the reduction of the supply electron-filled traps as the detrapping process goes on. Besides, for very high values of G the transition from the subthreshold to the on-state regime of the transistor and the consequent bending of the I_D-V_G transcharacteristics may also play a role on the growth of G. Similar data were collected for increasing pulse width and fixed $V_{G,read}$ (see fig. S3), where an increase of pulse width results in a stronger potentiation effect (see figs. S3, B and C, and S4).

To further assess the potentiation dynamics, we applied a sequence of pulses with random amplitude and fixed pulse width (see fig. S5). Figure 3E shows the applied pulse sequence while Fig. 3F shows the measured I_D after each pulse. The response I_D can be explained by both the applied pulse amplitude, which exponentially controls the potentiation (fig. S4), and the previous conductance state, which might induce saturation or decay effects at relatively large conductance. To better understand the I_D response behavior, Fig. 3G shows the measured $\Delta G = G_i - G_{i-1}$, defined as the difference between the conductance G_i measured after the application of the i-th pulse and the conductance G_{i-1} measured before the application of the same pulse (fig. S5). In Fig. 3G, the conductance change ΔG is reported as a function of the pulse amplitude of the i-th pulse and the conductance G_{i-1}. The device typically shows potentiation with $\Delta G > 0$ for $\Delta V_{G,pulse} < 0$ and depression with $\Delta G < 0$ for $\Delta V_{G,pulse} > 0$. This is highlighted in Fig. 3H, where all data of Fig. 3G are reported as a function of $\Delta V_{G,pulse}$. Data indicate an exponential increase of ΔG for decreasing $\Delta V_{G,pulse}$, which can be explained by the V_T shift after applying a negative $\Delta V_{G,pulse}$, combined with the exponential relationship between I_D and V_T in the subthreshold regime of the I-V curve of Fig. 2C. Also note the dependence on the initial conductance G_{i-1}, showing up as a higher depression or smaller potentiation for increasing G_{i-1} due to the lower number of electron-filled traps before the application of the gate pulse. These results are confirmed by similar experiments conducted on MoS_2-based CTM devices with 285-nm gate oxide (see fig. S6). A compact model of device potentiation and depression was developed on the basis of nonradiative multiphonon (NMP) model (*36*) and the Shockley-Read-Hall (SRH) model (*37*) (see figs. S7 to S9 and table S1). The surface potential in the MoS_2 channel of the CTM was calculated to determine the number of available electrons, which can be trapped (or detrapped) according to SRH and NMP rate equations. The relative V_T shift was calculated to evaluate the drain current I_D via drift/diffusion equations in the channel (see also note S1).

Neural signal processing

The nonlinear response in Figs. 2 and 3 can be adopted as the underlying processing mechanism in the reservoir layer of Fig. 1 for epileptiform events classification. To this end, we used local-field potential (LFP) signals collected via microelectrode array (MEA) from mouse horizontal hippocampus-entorhinal cortex (CTX) slices in which the epileptiform activity was acutely induced by 4-aminopyridine (4AP; 250 μM) (*38*). Figure 4A shows the brain slice coupled to the MEA, while Fig. 4 (B and C) shows the typical epileptiform patterns probed from the CTX and Cornu Ammonis 3 (CA3), respectively, consisting of ictal (seizure) and interictal (between seizures) events. In CTX, the ictal discharge is initiated by an interictal event followed

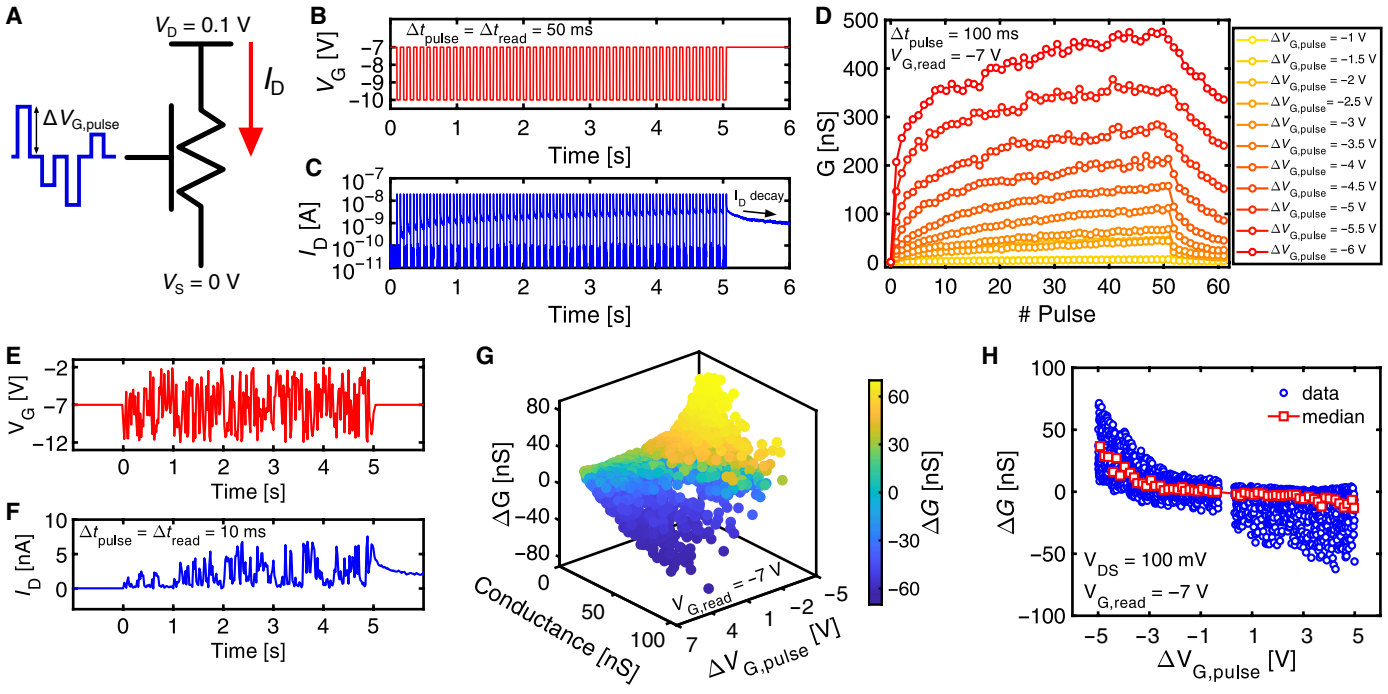

Fig. 3. CTM pulsed characteristics. (**A**) Sketch of the device and applied V_G pulses. V_S is normally kept to zero, while a constant V_{DS} allows for the measurement of the current I_D. (**B**) Negative-voltage pulse sequence applied to the gate of a CTM device with SiO_2 thickness of 90 nm. V_G is biased at a negative value ($V_{G,read} = -7$ V) to keep the device in the subthreshold region. The pulse time and read time were both set to $\Delta t_{pulse} = \Delta t_{read} = 50$ ms. (**C**) Corresponding I_D showing potentiation after each pulse. The drain current shows a time decay after the applied pulse train, due to the spontaneous electron detrapping. (**D**) Conductance values $G = I_D/V_{DS}$ measured during the read phase after each pulse for different amplitude $\Delta V_{G,pulse}$ of the pulse train. Larger potentiation is associated with larger $|\Delta V_{G,pulse}|$, although a saturation effect is observed for a relatively large amplitude for $|\Delta V_{G,pulse}| > 4$ V. After the 50 pulses, G points sampled at the same time interval of the pulses (100 ms) are plotted. (**E**) Random pulse waveform applied to the gate of a CTM device. (**F**) Corresponding I_D response for $\Delta t_{pulse} = \Delta t_{read} = 10$ ms. (**G**) Correlation plot of the conductance change $\Delta G = G_i - G_{i-1}$ as a function of the pulse amplitude $\Delta V_{G,pulse}$ and the conductance value G_{i-1} before each pulse. The saturation of the potentiation is observed for large conductance values, which also show larger depression (for $\Delta V_{G,pulse} > V_{G,read}$) compared to smaller device conductance values. (**H**) Correlation plot of ΔG as a function of $\Delta V_{G,pulse}$, showing the exponential voltage dependence of the potentiation.

by a post-ictal state of electrical silence due to postdischarge refractoriness. It is important to note that the interictal events recorded from the CTX and from the CA3 are distinct electrophysiological entities, referred to as "slow" and "fast" interictal pattern, respectively. These have been shown to originate from different synaptic mechanisms and exert opposite roles in this model of ictogenesis. Namely, the slow interictal has been shown to promote ictal discharge generation (cf. Fig. 4B), whereas the fast interictal has been shown to restrain it (*39*). Given the potential application of distinguishing the two types of events for seizure prediction and control, we have tested the performance of the CTM devices in their classification as distinct entities.

The main features of the epileptiform signals were classified by applying the signals to the gate of the CTM after proper amplification and measuring the response I_D. Note that all the prerecorded signals have been already labeled by trained neuroscientists. Figure 4D shows the epileptiform signals recorded via MEA and Fig. 4E shows the corresponding response I_D for four scenarios, namely, (i) baseline, i.e., absence of electrographic (ictal or interictal) events, (ii) interictal events from CTX and (iii) from CA3, and (iv) ictal discharge from CTX. Signals were amplified with a negative gain and shifted to match the typical voltage range for potentiation in Fig. 3. Note that the gain factor was optimized to maximize the dynamic response of the device, while minimizing possible stress and degradation. As a result, the large negative-voltage spikes in the ictal event of Fig. 4D cause a significant potentiation which results in a relatively large increase of I_D. The total response ΔI_D at the end of the applied temporal signal can thus be viewed as a characteristic feature or biomarker of the epileptiform signal (*40*), similar to feature extraction by convolutional filters in convolutional neural networks (*41*). The extracted feature ΔI_D obtained from the CTM reservoir layer was then analyzed by a readout layer with standard machine learning algorithms, such as decision tree, support vector machine (SVM) or k-nearest neighbor (KNN), for classification (see Materials and Methods). These algorithms were selected for their computational simplicity to minimize the time and energy consumption to train the readout layer (*16*). To ensure a high-classification accuracy, ΔI_D in the CTM devices was collected in response to the same epileptiform signals amplified by both a negative gain (Fig. 4, D and E) and a positive gain (see fig. S10). This allows to extract features of both the positive and the negative peaks of the signals thanks to the asymmetric characteristics in Fig. 3H, thus enhancing the robustness of the classification. Figure 4F shows the correlation plot of ΔI_D obtained in response to the signals in Fig. 4D with either positive or negative amplification. Each datapoint was obtained from the application of the signals to the same device, to evidence the stochastic variability of the device response (see fig. S11). In general, each class of activity results in a different cluster of data points with a clear separation among clusters, thus

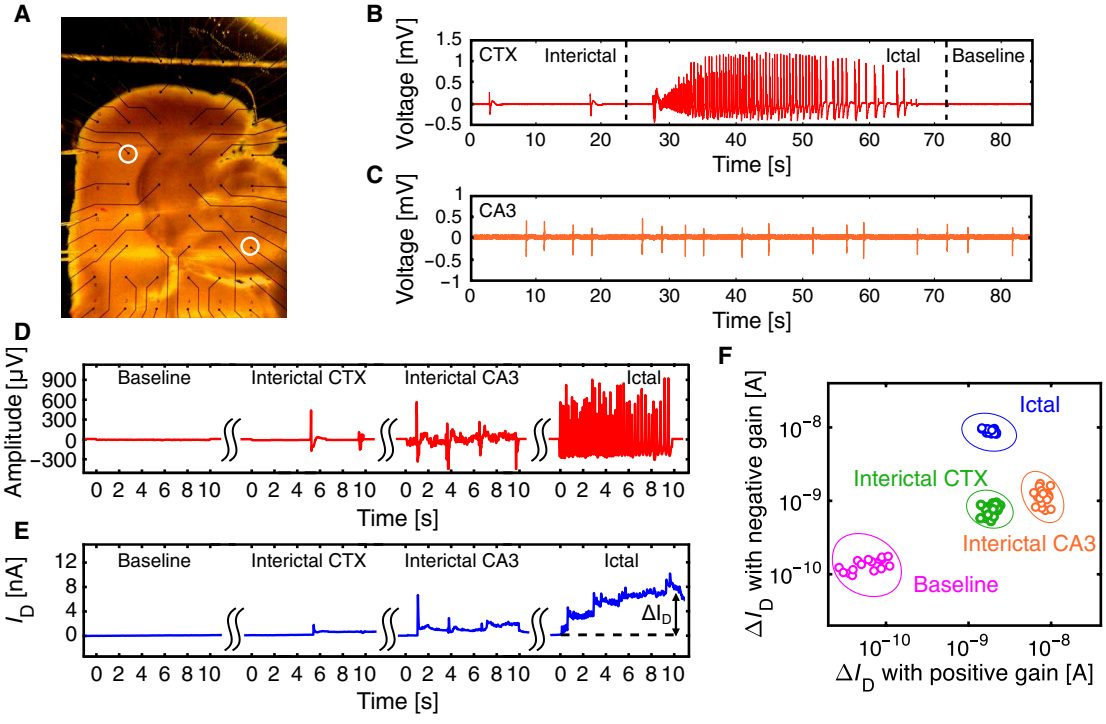

Fig. 4. CTM-based electrophysiological signal processing. (**A**) Optical micrograph of a mouse hippocampus-CTX slice coupled to a microelectrode array (MEA). The two electrodes used for signal acquisition in (B) and (C) are highlighted. (**B**) Epileptiform patterns recorded from the CTX, which include interictal and ictal discharges. Baseline refers to the absence of these two types of electrographic events. (**C**) Epileptiform patterns recorded from the hippocampal subfield Cornu Ammonis 3 (CA3), consisting here of a fast interictal pattern. (**D**) Epileptiform events used as input signals for the classification experiments. These signals were amplified by a negative gain $g = -1.85 \cdot 10^4$ and shifted by a voltage $V_{G,read} = -7$ V when applied to the gate of the CTM devices. (**E**) CTM current measured in response to the negatively amplified signals in (D). ΔI_D is the change of the drain current due to the integration process after the 10-s waveform. (**F**) Correlation plot of ΔI_D obtained with either positive or negative gain, demonstrating the ability of the CTM system to correctly classify the different epileptiform events. Note the separation between the "slow" interictal discharges (primarily generated by the CTX) and the fast interictal events intrinsically generated by the CA3.

confirming the ability to classify the different types of electrophysiological events.

To demonstrate the ability of the devices to provide a real-time classification of epileptiform events, the original MEA signal was applied to the gate of a device as shown in Fig. 5A. Here, each signal waveform was divided into segments of duration $\Delta t_{int} = 10$ s as in Fig. 4E, while the corresponding ΔI_D for each timeslot was collected (Fig. 5B). No reset pulses are applied between each segment, since the time needed for collecting the data by the instruments is enough for the spontaneous recovery of the initial state. The measured ΔI_D clearly shows a strong sensitivity and a clear response to the applied LFP. Signals were amplified with both negative (Fig. 5, A and B) and positive (fig. S12) gain to enable multiple feature extraction and maximize the classification accuracy. Figure 5C shows the correlation plot of ΔI_D from positive and negative amplification of MEA signals, demonstrating a clear separation between each cluster for each class of event.

Despite the ability to classify different types of events within the same signal, classification is achieved after a latency of 10 s in Fig. 5, which might be not sufficiently fast for closed-loop DBS. To support the ability to classify signals within a shorter latency, the real-time feature extraction was carried out for decreasing values of Δt_{int} (see fig. S13). Figure 5D shows the results of the analysis as a function of Δt_{int} for various readout algorithms in terms of accuracy, precision, and recall (see Materials and Methods for more details about algorithm implementation and the metrics extraction). A maximum accuracy of 97.52% was obtained by decision tree for $\Delta t_{int} = 10$ s (see table S2) although the accuracy drops by few % for shorter Δt_{int}, which highlights the intrinsic tradeoff between classification accuracy and latency. Other classification algorithms, such as KNN and SVM, show a better resilience for decreasing Δt_{int}. Figure 5E shows the confusion matrix for decision tree with $\Delta t_{int} = 10$ s (confusion matrices for other algorithms are reported in fig. S14). These results support the ability to properly discriminate between ictal and interictal events with a good classification accuracy.

Online in vitro experiments

Continuous-time experiments in the previous section were carried out by first collecting the MEA signals, then applying them off-line to the MoS_2-based CTM devices to validate their ability to classify the different epileptiform events. However, a fully convincing proof-of-concept demonstration would require collection and online in vitro classification of epileptiform patterns in the same experimental setup. To this purpose, we designed and developed a printed circuit board (PCB) hosting the MoS_2 CTM devices for the implementation of an online classification experiment (see fig. S15). Figure 6A shows the experimental setup, consisting of the PCB, the power supply, a digital oscilloscope and a control PC. The PCB can carry four chips, each chip holding four CTM devices (see fig. S16 and Materials and Methods). In this case, we used rodent primary hippocampal spheroids (Fig. 6B),

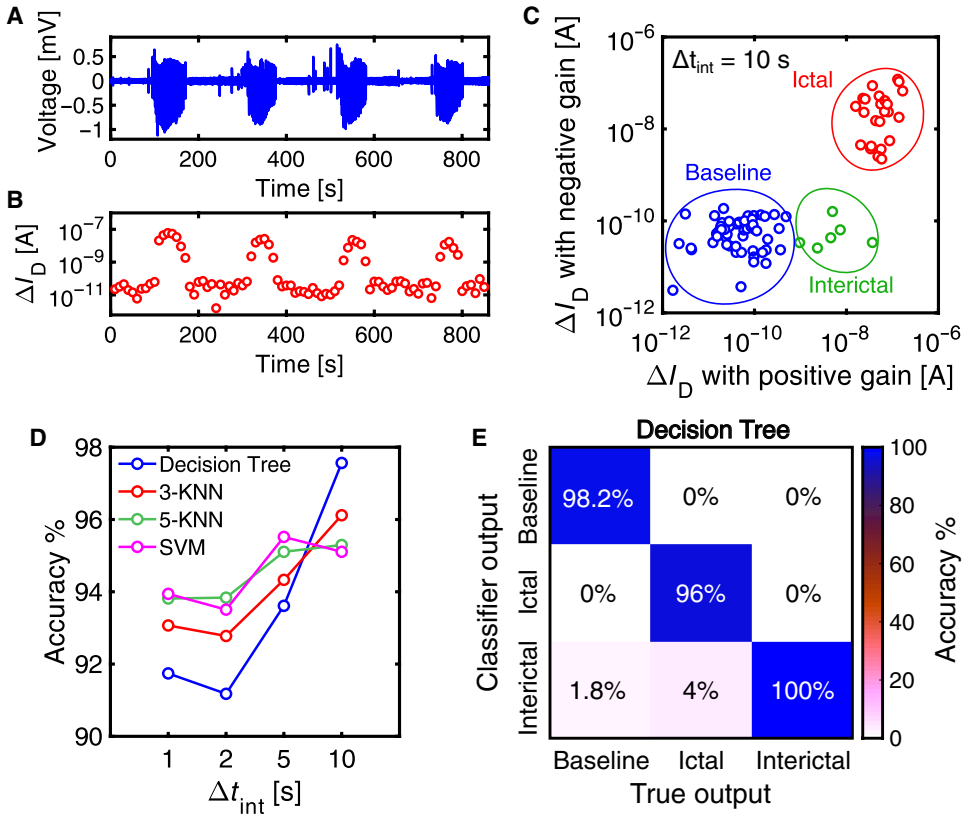

Fig. 5. Real-time epileptiform waveform processing. (**A**) LFP acquired via MEA from brain slices after inversion, or multiplication with −1. Ictal (seizure) events are clearly distinguishable by their amplitude prominence, intrinsic high frequency, and sustained (>20 s) duration; interictal events, recurring between ictal discharges, are shorted in duration and exhibit variable amplitude. (**B**) Corresponding device integration response for Δt_{int} = 10 s for negative amplified signal input. The device shows potentiation in correspondence of each ictal discharge. (**C**) Correlation plot showing the device current response (Δt_{int} = 10 s) for either positively or negatively amplified signal. The correlation plot indicates separate clusters, thus enabling classification of the epileptiform events. (**D**) Classification accuracy based on four machine-learning algorithms, namely decision tree, *k*-nearest neighbors with $k = 3$ and $k = 5$, and SVM, as a function of the device integration time Δt_{int}. (**E**) Confusion matrix for the classification obtained with the decision-tree algorithm and Δt_{int} = 10 s.

which have been shown to be spontaneously epileptogenic (*42*). The spheroid signal, amplified with either positive or negative gain, was applied as the input V_G to the CTM devices. The device was then read to obtain ΔI_D as the difference between the final and initial values of I_D measured at $V_{G,read}$. The CTM device was periodically initialized by applying a reset pulse every $\Delta t_{int} = 1$ s by a V_G pulse of amplitude $V_{G,reset} = 10$ V and pulse width $\Delta t_{reset} = 40$ ms (see fig. S17). The integration time Δt_{int} between two reset pulses was set to 1 s as a best trade-off between latency and accuracy of classification. The ictal discharge was detected by a simple comparison between the measured ΔI_D and a suitable threshold current I_{th}, which was carried out in the digital domain by a microcontroller. Note that signal detection might be in principle carried out in the analog domain by a comparator, thus avoiding the need of a microcontroller and enabling a fully analog, low-energy, in-sensor classification. To increase the robustness and the accuracy of the detection, the signal was applied to two devices in parallel with either positive or negative amplification. Seizure detection was marked by both devices exceeding their threshold current. To avoid false-positive detection, due to, e.g., interictal events, the condition $\Delta I_D > I_{th}$ had to be fulfilled twice in a row.

Figure 6C shows a typical spheroid signal recorded by a selected MEA channel exhibiting two ictal events. Note that the signal-to-noise ratio (SNR) is lower than in Fig. 5A, due to the nonoptimized MEA recording conditions, which could be improved by enhanced signal filtering. Figure 6D shows the detection signal g, where $g = 1$ corresponds to both devices exceeding their threshold, otherwise $g = 0$. From the figure, both ictal events were correctly detected with a latency shorter than 0.9 s. Note that the microcontroller needs approximately 60 ns to detect the seizure, while the read time is limited by the analog-digital conversion (ADC) speed, which in our case is 10 μs. Figure 6 (E and F) shows the response current ΔI_D of the two CTM devices with threshold current $I_{th,1} = 2.3$ nA and $I_{th,2} = 1.2$ nA, respectively. Ictal discharge detection with $\Delta t_{int} = 0.5$ s was also carried out (see fig. S18) by using a single device with alternating positive and negative gain. Thanks to the low currents of the subthreshold operated CTM, a low power consumption of only 2 nW/channel could be achieved (see Materials and Methods). A minimum latency of 0.8 s was demonstrated in online detection experiments (see fig. S18), thus supporting the feasibility of online ictal event detection for closed-loop DBS. The device data from the real-time experiment in Fig. 6 (E and F) were also classified using the same classification algorithms used in the experiments of Fig. 5D. The results, reported in table S3, demonstrate an overall acceptable accuracy of discrimination between ictal activities and baseline. The accuracy can be further improved by

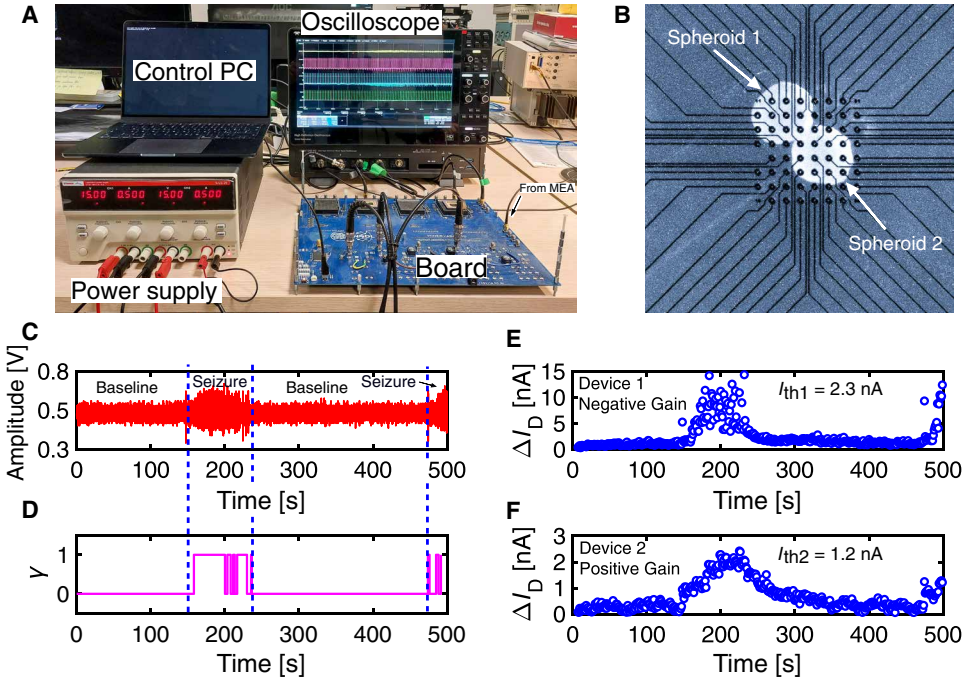

Fig. 6. Real-time seizure detection with CTM device in hippocampal spheroids. (**A**) Image of the experimental setup showing the custom-designed PCB which can accommodate up to 16 CTM devices and process up to four MEA channels in parallel. An oscilloscope is used for debugging. (**B**) Two hippocampal spheroids coupled to a MEA used for real-time experiments. (**C**) MEA signal at the input of the PCB showing two spontaneous ictal discharges. (**D**) Seizure bit g at the output of the detection system. The bit is raised when the device's current exceeds a threshold I_{th} (I_{th1} = 2.3 nA and I_{th2} = 1.2 nA). (**E**) Device 1 current response to the signal in (C) amplified with a negative gain. (**F**) Device 2 current response to the signal in (C) amplified with a positive gain.

properly adjusting the gain settings, which were optimized for early detection rather than classification purposes.

DISCUSSION

The ability to distinguish between interictal and ictal discharges is essential for the realization of closed-loop systems including sensing, processing, detection, and electrical stimulation (*5*). To this end, several requirements must be met, including (i) low power operation, to enable the integration of all functions within a single embedded system; (ii) small complexity, to minimize the circuit area/cost and facilitate the training of the system; (iii) high accuracy, to prevent false positive and false negative events; and (iv) short latency so that DBS can abort the seizure at its onset. Low-latency seizure onset detection is already implemented by the Food and Drug Administration (FDA)–approved responsive neurostimulation system, but the device is manually programmed by the physician across multiple sessions to tune the seizure detection parameters and the stimulation policy. The CTM-based approach described here, featuring the ability to classify epileptiform events as inherently coded in the device physics, may surpass the need of manually programming the seizure detection parameters by trial and error. The CTM devices could also distinguish different types of interictal events, supporting the possibility of seizure prediction. The latter would permit to prevent the seizure rather than aborting it at its onset, thus improving the therapeutic benefit for the patient.

To provide a fair benchmarking in terms of these criteria, Table 1 shows a summary of recently reported systems for seizure detection, including hardware concept based on both pure CMOS technology (*11*, *12*, *43*, *44*) and emerging memory and memristor devices (*8*, *12*, *18*, *20*, *45*). For a comprehensive comparison, Table 1 also includes a commercial closed-loop DBS system approved by the FDA (*3*) and an experimental closed-loop DBS system efficiently tested on animals (*46*). Hardware classification systems include ASICs (*43*) or CMOS-based SoC (*11*). However, to realize closed-loop DBS, an online approach with short latency is essential (*47*). Short-latency detection has been achieved with a spiking neural network implemented in a standard 180-nm CMOS technology (*44*), although without supporting the classification of ictal and interictal events and requiring a preprocessing of the biological signals for spike encoding. FPGA systems enable the implementation of a DNN for signal classification, thus achieving a good classification accuracy at the cost of a higher complexity, area, and power consumption (*8*, *9*).

Compared to the other reported systems, our work demonstrates real-time, online seizure detection based on emerging memory devices, low latency, high precision, and low power consumption. The adoption of an emerging memory based on a 2D semiconductors for the implementation of the seizure detector results in a small complexity, thanks to the reservoir network, and in an energy-efficient solution, thanks to the subthreshold operation of the CTM devices. A power consumption of only 2 nW/channel was estimated by assuming two MoS_2-based CTM devices for the classification of each channel. In addition, note that seizure classification can be achieved by a single comparator in the analog domain, which allows for the further simplification of the circuit by avoiding the energy-hungry

Table 1. Comparison of state-of-the-art systems for seizure detection.

Ref.	Supply voltages	Latency for detection	Real time	Ictal-interictal distinction	Dynamic power consumption	Emerging memories	Number of parameters	Area	Accuracy
(*8*)	1 V	Offline	No	No	>3 mW	Yes	3424 [Convolutional neural network (CNN) + fully connected (FC)]	FPGA area	98%
(*9*)	1.2 V	>10 s	No	No	>100 mW	No	96 (FC)	FPGA area	95.14%
(*10*)	2.5 V	≈5.9 s	No	Yes	14.91 mW	No	Filter +94,255 parameters (CNN + FC)	-	94.4%
(*11*)	1 V	≈6.7 s	No	-	3.5 μW	No	2 + kernel (SVM)	6.25 mm^2	-
(*12*)	5 V	Offline	No	No	≈1 nW (est)	Yes	-	2.8 μm^2 (single device)	-
(*18*)	2 V	≈2.4 s	No	No	60.81 nW/ channel	Yes	64 devices + latent dirichlet allocation (LDA) algorithm (2 parameters)	≈1000 μm^2 (array only)	95%
(*20*)	>4 V	>1.25 s	No	No	>200 nW/ channel	Yes	1 memristor +32 leaky integrate and fire (LIF) neurons per channel	1 μm^2 (single device)	96.4%
(*43*)	1.2 V	Offline	No	No	2.71 mW	No	2 + kernel (SVM algorithm)	0.2 mm^2	90.36%
(*44*)	0.250 V	229.4 ms	No	No	3.53 nW	No	30 spiking neurons +30 synapses + postprocessing algorithm	1.08 mm^2	-
(*45*)	>1 V	Offline	No	Yes	2.791 W	Yes	10,644 (CNN + FC)	31.255 mm^2	>99%
(*3*)	-	≈300 ms	Yes	Yes	≈5 μW/channel	No	5 (bandpass filter + line length + area detectors)	-	-
(*46*)	2.2 V	≈500 ms	Yes	Yes	5 μW/channel	No	2 filters +3 (SVM)	-	-
This work	13 V	<1 s*	Yes	Yes	≈2 nW/ channel + amplifier (see methods section)	Yes	2 (+2) / channel	100 nm^2 (single device) + amplifier	97.5% (Dec Tree, offline)

*Real-time experiment.

ADC. Despite the simplicity, our system displays a strong robustness for seizure classification, as demonstrated by the in situ real-time operation with nonideal conditions of low SNR.

In summary, we have demonstrated a seizure detection and classification system based on multilayer MoS_2 CTMs for RC with real-time, low-power operation. RC is enabled by the short-term memory behavior of the CTM devices originating from trapping/detrapping dynamics. The nonlinear integration of gate pulses and the decay behavior of the CTM device allow to classify electrophysiological signals, which is demonstrated with LFP signals collected from a mouse brain slice. Ictal, interictal, and baseline activities are classified within a latency of less than 10 s with 97.52% accuracy in offline mode, while real-time seizure detection was demonstrated within a latency of less than 1 s, thus validating MoS_2-based CTM devices for neuromorphic processing of neural signals for diagnostic, electroceutical, and human-machine interface.

MATERIALS AND METHODS

Fabrication of MoS_2-based charge trap memories

The p-doped silicon substrate was oxidized in a plasma-enhanced chemical vapor deposition system (STS Multiplex) at 300°C using SiH_4. The oxide thickness was 90 or 285 nm, measured by ellipsometry characterization (J.A. Woollam VASE ellipsometer). The

oxidized substrate was then cleaned with acetone and isoprophanol alcool using sonic bath, followed by the deposition of MoS_2 flakes by mechanical exfoliation. The patterning of source and drain terminals is then realized by electron beam lithography (LEO 1525 scanning electron microscope equipped with Raith Elphy and pattern generator system). Electrodes were made of Cr/Au (thickness 2/45 nm) deposited by thermal evaporation (Moorfield MINILAB-080). Typically, devices have 100 nm channel length, while gate oxide thickness can be either 90 or 285 nm. These values have been chosen to easily recognize exfoliated MoS_2 thin flakes via optical contrast.

Physical and electrical characterization of MoS_2-based CTM

Morphological characterization of the CTM was carried out by optical microscopy (Nikon Eclipse ME600) and SEM (Gemini LEO 1525). A probe station (Cascade Microtech Summit 12000) equipped with a semiconductor parameter analyzer (Keithley 4200A-SCS) was used to characterize the electrical properties of the MoS_2-CTM, both in DC and pulsed operation. A custom PCB was used for the real-time seizure detection experiments. The PCB is equipped with four PGA-121 sockets, which hold a single chip with a maximum of four devices. The PCB can process signals from a maximum of four MEA channels, each of which can be independently amplified and shifted. The board is also equipped with a microcontroller (STM32 F429ZI) to control all the peripherals, such as ADCs (for the readout), amplifier gains, switches, multiplexers (MUXs), and outputs. In a typical setup for real-time experiments, the signal coming from the MEA is properly amplified and shifted (and rectified) to be fed to the device gate. Here, a sequencer (made by a MUX) switches the gate between the amplified MEA signal, the reset signal, and the read voltage. Note that the signal coming from the MEA was filtered with a fourth order low-pass filter with a 50 Hz bandwidth and a high-pass filter with a 0.1 Hz cutoff frequency before amplification and shift. The output current of each device is read by a transimpedance amplifier with a fixed gain and the output voltage is read by an ADC. The microcontroller is used to set scheduler timing, ADC parameters, amplifier gains (changed by digital potentiometers), and storing output data. In addition, the detection of the seizure is displayed by the rise of an output bit (connected to a light-emitting diode), with a rule implemented in the microcontroller.

MEA electrophysiology

Horizontal hippocampus-CTX slices (400 mm thick) were prepared from male CD1 mice 4 to 8 weeks old. Epileptiform activity in brain slices was acutely induced by treatment with the convulsant drug 4AP (250 mm). Electrophysiological recordings were acquired via planar MEAs (TiN electrodes; layout, 6 × 10; electrode diameter, 30 mm; interelectrode distance, 500 mm; nominal electrode impedance, <100 kilohms). The MEA was coupled to a MEA1060 amplifier. Signals were sampled at 2 kHz (low-pass filtered at 1 kHz before digitization) and stored on the computer hard drive for offline analysis. Recordings were performed at 32°C. Full details on brain slice preparation, maintenance, and MEA recording can be found in (*38*). For experiments using the CTMs, the signals were bandpass filtered at (0.5 to 40 Hz) to remove the slow baseline drifts and the power-line noise (50 Hz), respectively.

Hippocampal spheroids were obtained from Sprague-Dawley rat embryos of both sexes (embryonic age, E17.5). The full details for hippocampal spheroid preparation and maintenance can be found in (*42*). Electrophysiological recordings were acquired via 3D MEAs (TiN electrodes; layout, 8 × 8; electrode diameter, 12 μm; height, 80 μm; interelectrode distance, 200 μm; nominal electrode impedance, ~150 kilohms). The MEA was coupled to a MEA2100-mini-HS60 amplifier connected to the IFB version 3.0 multiboot interface board through the signal collector unit. Hippocampal spheroids were not treated with any convulsant manipulation since they exhibit spontaneous epileptogenesis (*40*). The experimental temperature was controlled by a TC02 thermostat and checked with a k-type thermocouple for all MEA experiments. The equipment for MEA recording and temperature control was purchased from Multichannel Systems, Reutlingen, Germany.

All the electrophysiological signals were labeled by trained neuroscientist according to the following criteria:

1) Ictal events were identified as sustained (>10 s) discharges characterized by an initial fast oscillatory activity (tonic phase) followed by gradually slowing population bursts (clonic-like phase).

2) Interictal events were identified as short (<2 s) transients or population bursts recurring between ictal events.

3) Baseline is any signal segment devoid of both ictal and interictal events.

4) The onset and termination of epileptiform discharges were marked asymptotically, i.e., as first deflection and return to the baseline, respectively.

Classifier implementation

All the classifiers' algorithms were implemented in MATLAB. The input dataset using for training and testing are the ΔI_D points coming from the CTM signal integration and their corresponding labels (baseline, interictal, or ictal). Each integration time was processed separately. Each algorithm was trained using 80% of the dataset, with the remaining 20% reserved for testing.

Classifier performances extraction

We extracted the classification performance of the reservoir layer in terms of accuracy, precision, and recall. Accuracy is defined as the number of correct predictions (true positive TP + true negative TN) divided by the total number of predictions. Precision is the number of correct positive predictions (TP) divided by the total number of instances the algorithm predicted as positive (TP + false positives FP). Recall is the number of TP with respect to the total number of positive instances in the datasets (TP + false negative FN). Since we have three classes of instance (baseline, interictal, and ictal), we calculated the metrics for each class in a one-versus-all encoding, and we extracted the weighted average to have a single representative value of the classifier.

Compact modeling

The CTM compact model is realized in Matlab as follows. The first step is the solution of the 2D surface potential of the MoS_2-FET, which allows for the calculation of the number of free electrons available in the channel depending on the gate voltage with low computational cost. The density of electrons is also important to describe the dynamic of charge trapping. The dynamics of trap-filling is described through a two-site rate equation where the capture/emission coefficients are derived from the NMP model and the SRH model. Depending on the temporal evolution of gate voltage $V_G(t)$, the electrons in the channel can be trapped or emitted by the trap states trying to reach the new equilibrium condition. In the model, we track the amount of NMP-filled trap $f(t)$ and

SRH-filled traps $v(t)$, and then we can follow the corresponding $V_T(t)$ shift from purely electrostatic considerations. The temporal behavior of the threshold voltage $V_T(t)$ is then fed in the drift and diffusion relationships of the drain-source current I_{DS} to obtain the temporal current evolution.

Power consumption calculation

The power consumption of the MoS_2-based CTM is calculated considering the current flowing in the channel when the device is already potentiated (worse condition). During the seizure, for different experiments, we observed different values of current. We took a representative value $I_D = 10$ nA. Considering a read voltage of 100 mV the power consumption can be calculated as $10\ nA \cdot 100\ mV = 1$ nW. Using two devices per channel, we obtain a power consumption of 2 nW/channel. In addition, we also estimated the dynamic power consumption due to pulses at the gate. Considering a device with $W = 100$ nm, $L = 100$ nm, and $t_{ox} = 90$ nm, we can calculate the gate capacitance as $C = \varepsilon \cdot W{\cdot}L/t_{ox} = 3.8$ aF. The dynamic power can be calculated as $(5\ V)^2 \cdot 40\ Hz \cdot C = 3.83$ fW, which is negligible respect to the power consumption due to the drain current. To include the contribution by the preprocessing amplifier, we can refer to the two-stage amplifier described in (*48*), which is implemented using 90-nm CMOS technology. To reduce area and power consumption, this amplifier could potentially be realized in a more advanced 14-nm CMOS technology. On the basis of the data from (*48*) and assuming a CTM gate capacitance of 3.8 aF, we estimate that the amplifier could occupy an area of 51 μm^2, with a leakage power consumption of 21.2 pW and a dynamic power consumption of approximately 0.14 pW. The amplifier feedback network can be tailored to provide an additional power consumption of around 1 nW, which is equivalent to 50% of the CTM power consumption reported in Table 1.

Ethical approval

Experimental procedures involving animals were approved by the Italian Institute of Technology Animal Welfare body and by the Italian Ministry of Health (authorization no. 860/215-PR, approval date, 24 August 2015; and 176AA.NTN9, approval date 20 October 2018), in accordance with the National Legislation (D.Lgs. 26/2014) and the European Directive 2010/63/EU. Animals were purchased from Charles River, Italy. All efforts were made to minimize the number of used animals and their suffering.

Supplementary Materials

This PDF file includes:

Supplementary Note S1
Figs. S1 to S18
Tables S1 to S3
References

REFERENCES AND NOTES

1. E. Beghi, G. Giussani, E. Nichols, F. Abd-Allah, J. Abdela, A. Abdelalim, H. N. Abraha, M. G. Adib, S. Agrawal, F. Alahdab, A. Awasthi, Y. Ayele, M. A. Barboza, A. B. Belachew, B. Biadgo, A. Bijani, H. Bitew, F. Carvalho, Y. Chaiah, A. Daryani, H. P. Do, M. Dubey, A. Y. Y. Endries, S. Eskandarieh, A. Faro, F. Farzadfar, S.-M. Fereshtehnejad, E. Fernandes, D. O. Fijabi, I. Filip, F. Fischer, A. K. Gebre, A. G. Tsadik, T. G. Gebremichael, K. E. Gezae, M. Ghasemi-Kasman, K. G. Weldegwergs, M. G. Degefa, E. V. Gnedovskaya, T. B. Hagos, A. Haj-Mirzaian, A. Haj-Mirzaian, H. Y. Hassen, S. I. Hay, M. Jakovljevic, A. Kasaeian, T. D. Kassa, Y. S. Khader, I. Khalil, E. A. Khan, J. Khubchandani, A. Kisa, K. J. Krohn, C. Kulkarni, Y. L. Nirayo, M. T. Mackay, M. Majdan, A. Majeed, T. Manhertz, M. M. Mehndiratta, T. Mekonen, H. G. Meles, G. Mengistu, S. Mohammed, M. Naghavi, A. H. Mokdad, G. Mustafa, S. S. N. Irvani, L. H. Nguyen, M. R. Nixon, F. A. Ogbo, A. T. Olagunju, T. O. Olagunju, M. O. Owolabi, M. R. Phillips, G. D. Pinilla-Monsalve, M. Qorbani, A. Radfar, A. Rafay, V. Rahimi-Movaghar, N. Reinig, P. S. Sachdev, H. Safari, S. Safari, S. Safiri, M. A. Sahraian, A. M. Samy, S. Sarvi, M. Sawhney, M. A. Shaikh, M. Sharif, G. Singh, M. Smith, C. E. I. Szoeke, R. Tabarés-Seisdedos, M.-H. Temsah, O. Temsah, M. Tortajada-Girbés, B. X. Tran, A. A. T. Tsegay, I. Ullah, N. Venketasubramanian, R. Westerman, A. S. Winkler, E. M. Yimer, N. Yonemoto, V. L. Feigin, T. Vos, C. J. L. Murray, Global, regional, and national burden of epilepsy, 1990–2016: A systematic analysis for the Global Burden of Disease Study 2016. *Lancet Neurol.* **18**, 357–375 (2019).
2. M. J. Brodie, S. J. E. Barry, G. A. Bamagous, J. D. Norrie, P. Kwan, Patterns of treatment response in newly diagnosed epilepsy. *Neurology* **78**, 1548–1554 (2012).
3. R. Shankar, X. L. Marston, V. Danielson, B. Do Rego, R. Lasagne, O. Williams, L. Groves, Real-world evidence of epidemiology, patient characteristics, and mortality in people with drug-resistant epilepsy in the United Kingdom, 2011–2021. *J. Neurol.* **271**, 2473–2483 (2024).
4. B. C. Jobst, R. Kapur, G. L. Barkley, C. W. Bazil, M. J. Berg, G. K. Bergey, J. G. Boggs, S. S. Cash, A. J. Cole, M. S. Duchowny, R. B. Duckrow, J. C. Edwards, S. Eisenschenk, A. J. Fessler, N. B. Fountain, E. B. Geller, A. M. Goldman, R. R. Goodman, R. E. Gross, R. P. Gwinn, C. Heck, A. A. Herekar, L. J. Hirsch, D. King-Stephens, D. R. Labar, W. R. Marsh, K. J. Meador, I. Miller, E. M. Mizrahi, A. M. Murro, D. R. Nair, K. H. Noe, P. W. Olejniczak, Y. D. Park, P. Rutecki, V. Salanova, R. D. Sheth, C. Skidmore, M. C. Smith, D. C. Spencer, S. Srinivasan, W. Tatum, P. Van Ness, D. G. Vossler, R. E. Wharen, G. A. Worrell, D. Yoshor, R. S. Zimmerman, T. L. Skarpaas, M. J. Morrell, Brain-responsive neurostimulation in patients with medically intractable seizures arising from eloquent and other neocortical areas. *Epilepsia* **58**, 1005–1014 (2017).
5. M. Parastarfeizabadi, A. Z. Kouzani, Advances in closed-loop deep brain stimulation devices. *J. Neuroeng. Rehabil.* **14**, 79 (2017).
6. Y. Wei, J. Zhou, Y. Wang, Y. Liu, Q. Liu, J. Luo, C. Wang, F. Ren, L. Huang, A review of algorithm & hardware design for AI-based biomedical applications. *IEEE Trans. Biomed. Circuits Syst.* **14**, 145–163 (2020).
7. A. Subasi, J. Kevric, M. Abdullah Canbaz, Epileptic seizure detection using hybrid machine learning methods. *Neural Comput. Applic.* **31**, 317–325 (2019).
8. J. Zhang, H. Xu, H. Long, K. Hou, Z. Li, Z. Yang, Y. Wang, Q. Li, "EEG signal epilepsy detection system based on convolutional neural network and memristor array" in *2021 IEEE 4th International Conference on Electronics Technology* (ICET) pp. 851–855.
9. R. Sarić, D. Jokić, N. Beganović, L. G. Pokvić, A. Badnjević, FPGA-based real-time epileptic seizure classification using artificial neural network. *Biomed. Signal Process. Control* **62**, 102106 (2020).
10. Y. H. Liu, L. Chen, X. W. Li, Y. C. Wu, S. Liu, J. J. Wang, S. G. Hu, Q. Yu, T. P. Chen, Y. Liu, Epilepsy detection with artificial neural network based on as-fabricated neuromorphic chip platform. *AIP Advances* **12**, 035106 (2022).
11. N. Verma, A. Shoeb, J. Bohorquez, J. Dawson, J. Guttag, A. P. Chandrakasan, A micro-power EEG acquisition SoC with integrated feature extraction processor for a chronic seizure detection system. *IEEE J. Solid State Circ.* **45**, 804–816 (2010).
12. S. Subbulakshmi Radhakrishnan, A. Sebastian, A. Oberoi, S. Das, S. Das, A biomimetic neural encoder for spiking neural network. *Nat. Commun.* **12**, 2143 (2021).
13. X. Zhu, Q. Wang, W. D. Lu, Memristor networks for real-time neural activity analysis. *Nat. Commun.* **11**, 2439 (2020).
14. H. G. Rey, C. Pedreira, R. Quian Quiroga, Past, present and future of spike sorting techniques. *Brain Res. Bull.* **119**, 106–117 (2015).
15. S. Luan, I. Williams, M. Maslik, Y. Liu, F. De Carvalho, A. Jackson, R. Q. Quiroga, T. G. Constandinou, Compact standalone platform for neural recording with real-time spike sorting and data logging. *J. Neural Eng.* **15**, 046014 (2018).
16. M. Yan, C. Huang, P. Bienstman, P. Tino, W. Lin, J. Sun, Emerging opportunities and challenges for the future of reservoir computing. *Nat. Commun.* **15**, 2056 (2024).
17. D. Ielmini, Z. Wang, Y. Liu, Brain-inspired computing via memory device physics. *APL Mater.* **9**, 050702 (2021).
18. Z. Liu, J. Tang, B. Gao, X. Li, P. Yao, Y. Lin, D. Liu, B. Hong, H. Qian, H. Wu, Multichannel parallel processing of neural signals in memristor arrays. *Sci. Adv.* **6**, eabc4797 (2020).
19. Y. Chien, H. Xiang, Y. Shi, N. T. Duong, S. Li, K. Ang, A MoS_2 hafnium oxide based ferroelectric encoder for temporal-efficient spiking neural network. *Adv. Mater.* **35**, e2204949 (2023).
20. Z. Yang, K. Liu, R. Yuan, X. Wu, L. Cai, T. Zhang, Y. Tao, Y. Jin, Y. Yang, Seizure detection using dynamic memristor-based reservoir computing and leaky integrate-and-fire neuron for post-processing. *APL Machine Learning* **1**, 046123 (2023).
21. D. Wang, A. Yuan, S. Dai, X. Tang, K. Huang, S. Wei, H. Zhang, Z. Wang, A liquid optical memristor using photochromic effect and capillary effect. *Neuromorph. Comput. Eng.* **4**, 034003 (2024).
22. X. Wu, S. Wang, W. Huang, Y. Dong, Z. Wang, W. Huang, Wearable in-sensor reservoir computing using optoelectronic polymers with through-space charge-transport characteristics for multi-task learning. *Nat. Commun.* **14**, 468 (2023).

23. D. Jayachandran, R. Pendurthi, M. U. K. Sadaf, N. U. Sakib, A. Pannone, C. Chen, Y. Han, N. Trainor, S. Kumari, T. V. Mc Knight, J. M. Redwing, Y. Yang, S. Das, Three-dimensional integration of two-dimensional field-effect transistors. *Nature* **625**, 276–281 (2024).
24. B. Radisavljevic, A. Radenovic, J. Brivio, V. Giacometti, A. Kis, Single-layer MoS_2 transistors. *Nature Nanotech* **6**, 147–150 (2011).
25. Y.-Y. Chung, W.-S. Yun, B.-J. Chou, C.-F. Hsu, S.-M. Yu, G. Arutchelvan, M.-Y. Li, T.-E. Lee, B.-J. Lin, C.-Y. Li, A. Wei, D. M. Sathaiya, C.-T. Chung, S.-L. Liew, V. D.-H. Hou, W.-H. Chang, B.-H. Liu, C.-W. Chen, C.-Y. Su, C.-C. Kei, J. Cai, C.-C. Wu, J. Wu, T.-Y. Lee, C.-H. Chien, C.-C. Cheng, I. P. Radu, "Monolayer-MoS_2 stacked nanosheet channel with C-type metal contact" in *2023 International Electron Devices Meeting (IEDM)* (IEEE, San Francisco, CA, USA, 2023), pp. 1–4.
26. C. J. Dorow, T. Schram, Q. Smets, K. P. O'Brien, K. Maxey, C.-C. Lin, L. Panarella, B. Kaczer, N. Arefin, A. Roy, R. Jordan, A. Oni, A. Penumatcha, C. H. Naylor, M. Kavrik, D. Cott, B. Graven, V. Afanasiev, P. Morin, I. Asselberghs, C. J. Lockhart De La Rosa, G. Sankar Kar, M. Metz, U. Avci, "Exploring manufacturability of novel 2D channel materials: 300 mm wafer-scale 2D NMOS & PMOS using MoS_2, WS_2, & WSe_2" in *2023 International Electron Devices Meeting (IEDM)* (IEEE, San Francisco, CA, USA, 2023), pp. 1–4.
27. G. Migliato Marega, H. G. Ji, Z. Wang, G. Pasquale, M. Tripathi, A. Radenovic, A. Kis, A large-scale integrated vector–matrix multiplication processor based on monolayer molybdenum disulfide memories. *Nat. Electron.* **6**, 991–998 (2023).
28. R. Xu, H. Jang, M.-H. Lee, D. Amanov, Y. Cho, H. Kim, S. Park, H. Shin, D. Ham, Vertical MoS_2 double-layer memristor with electrochemical metallization as an atomic-scale synapse with switching thresholds approaching 100 mV. *Nano Lett.* **19**, 2411–2417 (2019).
29. V. K. Sangwan, H.-S. Lee, H. Bergeron, I. Balla, M. E. Beck, K.-S. Chen, M. C. Hersam, Multi-terminal memtransistors from polycrystalline monolayer molybdenum disulfide. *Nature* **554**, 500–504 (2018).
30. M. Farronato, M. Melegari, S. Ricci, S. Hashemkhani, A. Bricalli, D. Ielmini, Memtransistor devices based on MoS_2 multilayers with volatile switching due to Ag cation migration. *Adv. Electron Mater.* **8**, 2101161 (2022).
31. M. Farronato, P. Mannocci, M. Melegari, S. Ricci, C. M. Compagnoni, D. Ielmini, Reservoir computing with charge-trap memory based on a MoS_2 channel for neuromorphic engineering. *Adv. Mater.* **35**, 2205381 (2023).
32. Y. Y. Illarionov, G. Rzepa, M. Waltl, T. Knobloch, A. Grill, M. M. Furchi, T. Mueller, T. Grasser, The role of charge trapping in MoS_2/SiO_2 and MoS_2/hBN field-effect transistors. *2D Mater.* **3**, 035004 (2016).
33. Y. Y. Illarionov, T. Knobloch, M. Waltl, G. Rzepa, A. Pospischil, D. K. Polyushkin, M. M. Furchi, T. Mueller, T. Grasser, Energetic mapping of oxide traps in MoS^2 field-effect transistors. *2D Mater.* **4**, 025108 (2017).
34. A. Di Bartolomeo, L. Genovese, F. Giubileo, L. Iemmo, G. Luongo, T. Foller, M. Schleberger, Hysteresis in the transfer characteristics of MoS2 transistors. *2D Mater.* **5**, 015014 (2017).
35. M. Farronato, M. Melegari, S. Ricci, S. Hashemkani, C. M. Compagnoni, D. Ielmini, "Low-current, highly linear synaptic memory device based on MoS_2 transistors for online training and inference" in *2022 IEEE 4th International Conference on Artificial Intelligence Circuits and Systems (AICAS)* (IEEE, Incheon, Korea, Republic of, 2022), pp. 1–4.
36. T. Grasser, Stochastic charge trapping in oxides: From random telegraph noise to bias temperature instabilities. *Microelectron. Reliab.* **52**, 39–70 (2012).
37. W. Shockley, W. T. Read, Statistics of the recombinations of holes and electrons. *Phys. Rev.* **87**, 835–842 (1952).
38. G. Panuccio, I. Colombi, M. Chiappalone, Recording and modulation of epileptiform activity in rodent brain slices coupled to microelectrode arrays. *J. Vis. Exp.* 10.3791/57548 , 57548 (2018).
39. M. Avoli, M. D'Antuono, J. Louvel, R. Köhling, G. Biagini, R. Pumain, G. D'Arcangelo, V. Tancredi, Network and pharmacological mechanisms leading to epileptiform synchronization in the limbic system in vitro. *Prog. Neurobiol.* **68**, 167–207 (2002).
40. R. Midya, Z. Wang, S. Asapu, X. Zhang, M. Rao, W. Song, Y. Zhuo, N. Upadhyay, Q. Xia, J. J. Yang, Reservoir computing using diffusive memristors. *Adv. Intell. Syst.* **1**, 1900084 (2019).
41. Y. Lecun, L. Bottou, Y. Bengio, P. Haffner, Gradient-based learning applied to document recognition. *Proc. IEEE* **86**, 2278–2324 (1998).
42. J. W. Ephraim, D. Caron, A. Canal-Alonso, J. M. Corchado, G. Palazzolo, G. Panuccio, Developing hippocampal spheroids model ictogenesis and epileptogenesis. [Preprint] (2023).
43. H. Elhosary, M. H. Zakhari, M. A. Elgammal, M. A. Abd El Ghany, K. N. Salama, H. Mostafa, Low-power hardware implementation of a support vector machine training and classification for neural seizure detection. *IEEE Trans. Biomed. Circuits Syst.* **13**, 1324–1337 (2019).
44. M. Ronchini, Y. Rezaeiyan, M. Zamani, G. Panuccio, F. Moradi, NET-TEN: A silicon neuromorphic network for low-latency detection of seizures in local field potentials. *J. Neural Eng.* **20**, 036002 (2023).
45. C. Li, C. Lammie, X. Dong, A. Amirsoleimani, M. R. Azghadi, R. Genov, Seizure detection and prediction by parallel memristive convolutional neural networks. *IEEE Trans. Biomed. Circuits Syst.* **16**, 609–625 (2022).
46. S. Stanslaski, P. Afshar, P. Cong, J. Giftakis, P. Stypulkowski, D. Carlson, D. Linde, D. Ullestad, A.-T. Avestruz, T. Denison, Design and validation of a fully implantable, chronic, closed-loop neuromodulation device with concurrent sensing and stimulation. *IEEE Trans. Neural Syst. Rehabil. Eng.* **20**, 410–421 (2012).
47. P. Handa, E. Gupta, S. Muskan, N. Goel, A review on software and hardware developments in automatic epilepsy diagnosis using EEG datasets. *Exp. Syst.* **40**, e13374 (2023).
48. Nidhi, N., Prasad, D., Nath, V. A high-performance energy-efficient 75.17 dB two-stage operational amplifier. Nath, V., Mandal, J. (Eds) Nanoelectronics, Circuits and Communication Systems. Lecture Notes in *Electrical Engineering*. (Springer, Singapore, 2019), vol 511.
49. J. Zeng, W. Deng, C. Zhou, J. Peng, J. Huang, A compact model of MoS_2 field-effect transistors from drift-diffusion to ballistic carrier transport regimes. *IEEE J. Electron Devices Soc.* **8**, 285–290 (2020).
50. D. Ielmini, M. Manigrasso, F. Gattel, M. G. Valentini, A new NBTI model based on hole trapping and structural relaxation in MOS dielectrics. *IEEE Trans. Electron. Devices* **56**, 1943–1952 (2009).
51. Y. Park, H. W. Baac, J. Heo, G. Yoo, Thermally activated trap charges responsible for hysteresis in multilayer MoS_2 field-effect transistors. *Appl. Phys. Lett.* **108**, 083102 (2016).
52. K. Choi, S. R. A. Raza, H. S. Lee, P. J. Jeon, A. Pezeshki, S.-W. Min, J. S. Kim, W. Yoon, S.-Y. Ju, K. Lee, S. Im, Trap density probing on top-gate MoS_2 nanosheet field-effect transistors by photo-excited charge collection spectroscopy. *Nanoscale* **7**, 5617–5623 (2015).

Acknowledgments: We want to thank all the Polifab (the micro- and nanotechnology infrastructure of Politecnico di Milano) staff for the help in the fabrication of the MoS_2-based CTM devices, G. Pruzzo for designing and making the custom incubator lid for spheroid MEA electrophysiology, M. Nanni and A. De Benedetti for the technical help for the preparation of the spheroids. **Funding:** This article has received funding from the European Union (EU) under the H2020 Future and Emerging Technologies program (grant 824164) and from the European Research Council (ERC) under the European Union's Horizon Europe Research and Innovation Programme (grant 101054098). **Author contributions:** Conceptualization: G.P. and D.I. Methodology: M.F., P.M., A.M., G.P., and D.I. Investigation: M.F., P.M., A.M., A.A., M.C., and A.B. Visualization: M.F., A.M., and P.M. Supervision: M.F., G.P., and D.I. Writing–original draft: M.F., G.P., C.M.C., M.C., and D.I., Writing–review and editing: M.F., G.P., and D.I. **Competing interests:** The authors declare that they have no competing interests. **Data and materials availability:** All data are available in the main text and/or the Supplementary Materials. The datasets generated during and/or analyzed during the current study and the codes used for simulations are available in the following public repository: 10.5281/zenodo.13859574

Submitted 27 June 2024
Accepted 18 December 2024
Published 17 January 2025
10.1126/sciadv.adr3241